Detailed quasiclassical dynamics of the F⁻ + CH₃Br reaction on an *ab initio* analytical potential energy surface

(iD) **Viktor Tajti,** (iD) **Tibor Győri, and** (iD) **Gábor Czakó**

View Online   **Export Citation**   **CrossMark**

Detailed quasiclassical dynamics of the F⁻ + CH₃Br reaction on an *ab initio* analytical potential energy surface

View Online · Export Citation · CrossMark

Viktor Tajti, [iD] Tibor Győri, [iD] and Gábor Czakó[a) [iD]
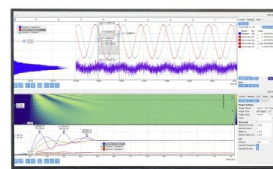
AFFILIATIONS

MTA-SZTE Lendület Computational Reaction Dynamics Research Group, Interdisciplinary Excellence Centre and Department of Physical Chemistry and Materials Science, Institute of Chemistry, University of Szeged, Rerrich Béla tér 1, Szeged H-6720, Hungary

a)Author to whom correspondence should be addressed: gczako@chem.u-szeged.hu

ABSTRACT

Dynamics and mechanisms of the $F^- + CH_3Br(v = 0) \rightarrow Br^- + CH_3F$ (S_N2 via Walden inversion, front-side attack, and double inversion), F^- + inverted-CH_3Br (induced inversion), $HF + CH_2Br^-$ (proton abstraction), and $FH \cdots Br^- + {}^1CH_2$ reactions are investigated using a high-level global *ab initio* potential energy surface, the quasiclassical trajectory method, as well as non-standard configuration- and mode-specific analysis techniques. A vector-projection method is used to identify inversion and retention trajectories; then, a transition-state-attack-angle-based approach unambiguously separates the front-side attack and the double-inversion retention pathways. The Walden-inversion S_N2 channel becomes direct rebound dominated with increasing collision energy as indicated by backward scattering, initial back-side attack preference, and the redshifting of product internal energy peaks in accord with CF stretching populations. In the minor retention and induced-inversion pathways, almost the entire available energy transfers into product rotation–vibration, and retention mainly proceeds with indirect, slow double inversion following induced inversion with about 50% probability. Proton abstraction is dominated by direct stripping (evidenced by forward scattering) with CH_3-side initial attack preference, providing mainly vibrationally ground state products with significant zero-point energy violation.

Published under an exclusive license by AIP Publishing. https://doi.org/10.1063/5.0065209

I. INTRODUCTION

Bimolecular nucleophilic substitution (S_N2) has a long history beginning with Walden's discovery of a stereospecific optical inversion process in 1896.[1] Later in the 1930s, Hughes and co-workers[2,3] described the atomic-level mechanisms of the S_N2 reactions, which usually follow a back-side attack Walden-inversion pathway via pre- and post-reaction ion–dipole complexes separated by an often submerged central transition state. Furthermore, a front-side attack retention pathway via a high barrier was also discussed in the early work.[4] In the 1970s, experiments started to investigate S_N2 reactions in the gas phase, focusing, in the first few decades, on kinetics and thermodynamics as well as spectroscopy of the ion–dipole complexes.[5–15] Following some early dynamics experiments,[16,17] in 2008, Mikosch *et al.*[18] developed a crossed-beam velocity-map imaging technique to investigate the collision

dynamics of ion–molecule reactions. For the first time, detailed scattering angle and product internal energy distributions could be measured, and the signatures of the direct rebound mechanism of S_N2 reactions could be observed.[18] Theoretical studies of S_N2 reactions also started in the 1970s with electronic structure computations for the stationary points,[19] followed by reaction dynamics simulations using direct quasiclassical dynamics and reduced-dimensional time-independent quantum dynamics.[20–28] In 2013, we initiated an analytical potential energy surface (PES)-based approach for S_N2 reactions by reporting a high-level full-dimensional *ab initio* analytical PES for the $F^- + CH_3Cl$ system.[29] Later, we developed global analytical PESs for several ion–molecule reactions, such as $F^- + CH_3F$,[30] $F^- + CH_3Br$,[31] $F^- + CH_3I$,[32] $OH^- + CH_3I$,[33] $F^- + NH_2Cl$,[34] and $F^- + CH_3CH_2Cl$.[35] These analytical PESs allow the use of higher-level electronic structure theory than direct dynamics and enable efficient dynamics

simulations using either the quasiclassical trajectory (QCT) or the time-dependent quantum method.[29–39] QCT computations on these PESs revealed a novel double-inversion mechanism,[40] front-side complex formation,[41,42] multiple-inversion pathway for N-centered S_N2 reactions,[34] and branching ratios for substitution and elimination (E2) processes,[35] as well as showed unprecedented agreement with experiments.[35,41,43]

On the one hand, the analytical PES-based approach is more accurate and more efficient than direct dynamics. On the other hand, this approach requires the development of the PES by (1) selecting a few tens of thousands of representative nuclear configurations, (2) performing *ab initio* computations, and (3) fitting the energy points by an appropriate functional form. These steps may be repeated iteratively until the desired accuracy is achieved. Recently, we developed a program system, called ROBOSURFER,[31] which automates the above procedure, enabling efficient PES developments. Since 2020, four of our S_N2 PESs ($F^- + CH_3Br$, $OH^- + CH_3I$, $F^- + NH_2Cl$, and $F^- + CH_3CH_2Cl$)[31,33–35] have been developed using ROBOSURFER besides the $F/Cl + C_2H_6$ PESs[44,45] and several ongoing work. The $F^- + CH_3Br$ reaction was used as a test system during the initial development of the ROBOSURFER program package. In our previous publication,[31] we focused on the methodological details of the program system, reported different PES versions for the $F^- + CH_3Br$ reaction, and monitored the integral cross sections obtained on the different PESs developed by various strategies. In the present work, we describe a detailed QCT analysis of the $F^- + CH_3Br$ reaction, revealing cross sections, reaction probabilities, scattering angle, initial attack angle, and product internal energy distributions for the S_N2 and proton-abstraction channels at different collision energies. Besides back-side attack Walden inversion, we also determine and characterize the front-side attack and double-inversion retention pathways, and we consider additional minor product channels, such as inverted CH_3Br and $FH\cdots Br^- + CH_2$. Furthermore, we report mode-specific polyatomic product vibrational distributions for the S_N2 and proton-abstraction channels. The computational details are described in Sec. II, and the detailed dynamics results are presented and discussed in Sec. III. The paper ends with summary and conclusions in Sec. IV.

II. COMPUTATIONAL DETAILS

We investigate the dynamics of the $F^- + CH_3Br(v = 0)$ reaction with the analysis of QCTs at collision energies (E_{coll}) of 7.4, 15.9, 35.3, 42.5, 50.0, and 60.0 kcal/mol. The trajectories were computed on a full-dimensional analytical explicitly-correlated coupled-cluster singles, doubles, and perturbative triples CCSD(T)-F12b/aug-cc-pVTZ-PP PES developed recently by ROBOSURFER and denoted as PES III in Ref. 31. The initial conditions of the QCT simulations were described in detail in Ref. 31. In short, the quasiclassical ground vibrational state ($v = 0$) of the reactant is prepared by standard normal-mode sampling,[46] and the impact parameter (b) varies from 0 to b_{max} with a step size of 0.5 bohr. There is no reactive collision if the impact parameter is greater than b_{max}. We analyze 5000 trajectories at every combination of E_{coll} and b; thus, the present study is based on 7×10^5 trajectories.

We distinguish the configuration retention of the product from inversion in the case of the S_N2 channel by applying a vector-projection scheme, which was introduced in Ref. 47. In brief, we

define a Cartesian coordinate system where the origin is the carbon atom, and we calculate the cross product of the position vectors of one of the hydrogen atoms and the halogen ligand, which results in a normal vector. Then, we evaluate the dot product of this normal vector and the difference of the position vectors of the other two hydrogen atoms. Dot-product values are calculated in the case of the initial (CH_3Br) and final (CH_3F) structures of the reactive S_N2 trajectories, and we compare the signs of the dot products with each other. The same and opposite signs mean retention and inversion, respectively. As proposed in Ref. 47, for the numerical identification of front-side attack (fs S_N2) or double inversion (di S_N2), we scan backward the trajectories until we find a transition state (TS) defined by the C–Br distance becoming less than 2.3 Å as the C–Br distances at the front-side attack and Walden-inversion TSs are 2.446 and 2.201 Å on the PES,[31] respectively. At this TS, we separate the front-side attack TS from the Walden-inversion TS (second TS of di S_N2) by applying a limit of 111° (based on Ref. 47 and some test computations as discussed in Sec. III) to the F–C–Br attack angle (γ). Thus, γ less than 111° corresponds to front-side attack, whereas γ greater than 111° defines double inversion.

For the integral cross section calculations, we apply soft and hard zero-point energy (ZPE) constraints. In the case of hard ZPE constraints, we discard trajectories (we consider them non-reactive) if the vibrational energy of either product is less than the corresponding harmonic ZPE. If we have a diatomic fragment, we compare the diatomic internal energy to the anharmonic ZPE corresponding to the given rotation state. The anharmonic rotational–vibrational levels of the HF molecule are taken from Ref. 48. In the soft case, the above constraints are applied to the sum of the product vibrational energies and the sum of the ZPEs; thus, inequalities of the hard case can compensate each other. For differential cross section-type distributions, no ZPE constraint is applied.

We perform mode-specific vibrational energy computations for the polyatomic products (CH_3F and CH_2Br^-) following the procedure described in detail in Ref. 49. The zeroth step of this method is to carry out normal-mode analysis for the optimized products to obtain the harmonic vibrational frequencies (ω_k) and normal-mode eigenvectors (ω_k). In the 1st step, we remove the angular momentum of the products by modifying velocities. Then, we use an Eckart transformation,[49,50] also considering H-atom permutations, to find the best overlap[51] between the optimized/reference and the actual/final structure. In the next step, we transform the mass-scaled Cartesian displacement coordinates and velocities by using the eigenvectors obtained in the zeroth step to determine the normal coordinates (Q_k) and momenta (P_k). Finally, we calculate the mode-specific harmonic vibrational energies (E_k) and the integer vibrational quantum numbers (n_k), in atomic units, as

$$E_k = P_k^2/2 + (\omega_k Q_k)^2/2, \tag{1}$$

$$n_k = \lfloor E_k/\omega_k \rfloor, \tag{2}$$

where the floor sign $\lfloor \rfloor$ denotes rounding down to an integer value and $k = 1, \ldots, 3N - 6$, where N is 5 and 4 for CH_3F and CH_2Br^-, respectively. For the diatomic HF product, rotational and vibrational quantum numbers are assigned as detailed in Refs. 48 and 45.

III. RESULTS AND DISCUSSION

The different reaction pathways and their energetics for the F^- + CH_3Br reaction are shown in Fig. 1. The S_N2 channel leading to Br^- + CH_3F is highly exothermic, $\Delta H_0 = -39.2$ kcal/mol, whereas the proton abstraction forming the HF + CH_2Br^- products is endothermic, $\Delta H_0 = 20.7$ kcal/mol. The S_N2 reaction can proceed with back-side attack Walden inversion via submerged hydrogen-bonded and ion–dipole minima (HMIN and PREMIN) connected by a hydrogen-bonded TS (HTS), followed by a Walden-inversion TS (WALDENTS) and a deep post-reaction ion–dipole minimum (POSTMIN), as shown in Fig. 1. Besides the traditional Walden inversion, the S_N2 reaction can also occur with retention of the initial configuration through a front-side attack TS (FSTS) or a double-inversion TS (DITS) having adiabatic barrier heights of 24.3 or 11.8 kcal/mol, respectively. The first step of double inversion is a proton-abstraction induced inversion, which may be followed by a second inversion via the WALDENTS. If this second substitution event does not occur, the first inversion (induced inversion) results in an inverted CH_3Br molecule. HF + CH_2Br^- formation proceeds via several minima and transition states, whose energy levels are below the product asymptote, as shown in Fig. 1.

The inversion and retention trajectories are identified using the vector-projection method, and the numerical separation of the front-side attack and double-inversion retention pathways is done based on the TS attack angles, as described in Sec. II. The TS attack angle distributions for the retention pathways are given in Fig. 2.
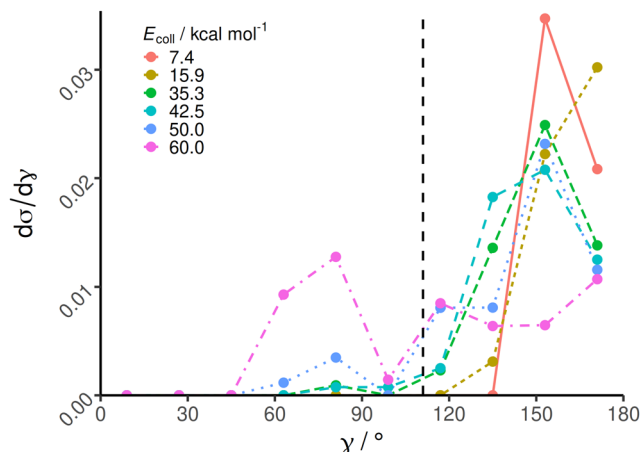

FIG. 2. Transition state attack angle distributions for the S_N2 retention F^- + CH_3Br trajectories at different collision energies. The dashed vertical line indicates an attack angle of 111° separating the front-side attack (left side) and double-inversion (right side) pathways.

At low collision energies, the γ distributions peak around 150°–180° corresponding to double inversion, and as E_{coll} increases, a second peak emerges around 80° as a fingerprint of front-side attack (the F–C–Br angle at FSTS is 80.3°). As shown in Fig. 2, a dividing limit
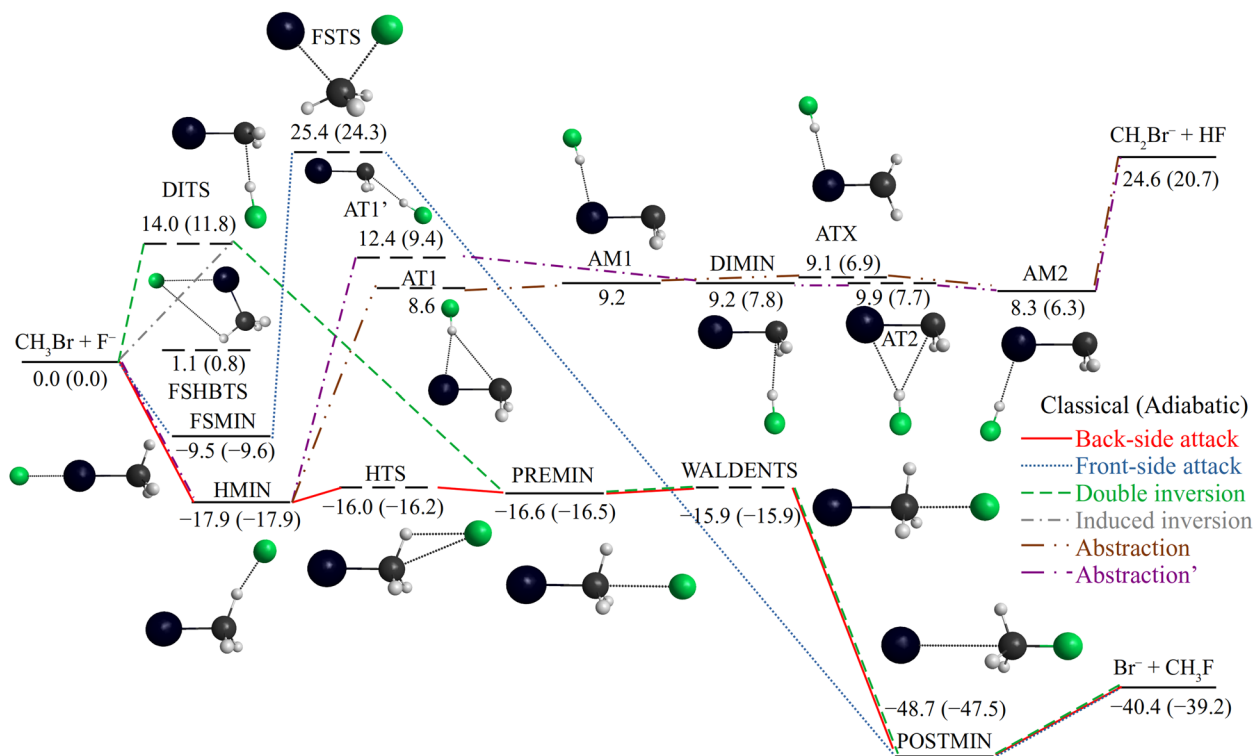

FIG. 1. Schematic potential energy surface for the F^- + CH_3Br S_N2 and proton-abstraction reactions showing the classical (ZPE-corrected adiabatic) relative energies in kcal/mol for the stationary points along the different reaction pathways corresponding to PES III of Ref. 31.

of 111° separates the front-side attack and double-inversion parts of the γ distributions with negligible uncertainties, similar to the case of the F⁻ + CH₃Cl/CH₃I reactions investigated in Ref. 47. We have tested that varying the dividing limit between 90° and 120° results in only around ±0.001 bohr² cross section uncertainties, which in most cases, especially for double inversion, correspond to relative errors less than 10%. Figure 3 shows the propagation time distributions of the front-side attack and double-inversion trajectories. As shown in the figure, front-side attack is more direct than double inversion as all the front-side attack trajectories finish within 6 ps, whereas the double-inversion time distributions are broad with a long tail beyond 10 ps. In our previous studies,[32,40,47] we found that in the case of F⁻ + CH₃Cl, one can distinguish between front-side attack (direct) and double inversion (indirect) based on integration time, whereas this time-based assignment is ambiguous for F⁻ + CH₃I. In the present F⁻ + CH₃Br case, integration time is also not a good indicator, like in F⁻ + CH₃I, because the overlap between the front-side attack and double-inversion time distributions is significant in the 2–6 ps range, as shown in Fig. 3. Animations of selected retention trajectories reveal that, besides the proton-abstraction induced inversion followed by the Walden inversion mechanism, double inversion can also occur via a methyl-tumbling-rotation pathway, where the internally hot CH₃F fragment produced by Walden inversion becomes inverted again in the exit channel by the turn of the CH₃ group.

Excitation functions (integral cross sections as a function of E_{coll}) and opacity functions (reaction probabilities as a function of b) for the different reaction channels and pathways are shown in Figs. 4 and 5, respectively. The back-side attack Walden-inversion S$_N$2 cross sections decrease with increasing E_{coll}, as expected in the case of an exothermic, barrier-less reaction. This is in accord with the opacity functions because the reaction probabilities and b_{max} values decrease with increasing E_{coll}, as shown in the upper panel of Fig. 5. The large b_{max} value at low E_{coll}, e.g., 15 bohr at E_{coll} = 7.4 kcal/mol, is due to the long-range attractive ion–dipole interactions in the entrance channel, which are counteracted by fast translational motion as E_{coll} increases. Front-side attack reactivity is zero at the lowest two collision energies (7.4 and 15.9 kcal/mol) and is open at

E_{coll} = 35.3 kcal/mol, as expected based on the barrier height of 24.3 kcal/mol. The front-side attack cross sections increase with increasing E_{coll}, and a sharp rise is seen between 50 and 60 kcal/mol, but the cross section is still only 0.01 bohr² at E_{coll} = 60 kcal/mol (Fig. 4). For comparison, the back-side attack S$_N$2 cross section is 4.98 bohr² at the same E_{coll}. This small front-side attack reactivity corresponds to less than 0.1% reaction probability and a low b_{max} value (b_{max} is usually less than 4 bohr), as shown in Fig. 5. Double inversion opens well below front-side attack (barrier height of the former is only 11.8 kcal/mol), and the double inversion cross section is already 0.04 bohr² at E_{coll} = 15.9 kcal/mol, becomes 0.07 bohr² at 35.3 kcal/mol, and then decreases with increasing E_{coll}. A similar double-inversion excitation function shape was found in our previous studies on the F⁻ + CH₃Cl/CH₃I reactions,[32,40] which may be explained by the fact that first, the collision energy is needed to activate the induced inversion over a positive barrier, but as E_{coll} increases, the extra translational energy counteracts the indirect double inversion process. The maxima of double-inversion cross sections are around 0.06 bohr² (Ref. 47), 0.07 bohr² (Fig. 4), and 0.30 bohr² (Ref. 47) for the F⁻ + CH₃Y reactions with Y = Cl, Br, and I, respectively, in accord with the decreasing barrier heights from Y = Cl to I. The F⁻ + CH₃Br double-inversion reaction probabilities are small but may go up to 0.6%, as shown in Fig. 5. The shape and magnitude of the induced-inversion and double-inversion excitation and opacity functions are very similar within the statistical uncertainty of these low-probability channels. This finding shows that a reactive substitution event via the WALDENTS occurs after induced inversion with a surprisingly high, about 50%, probability. In the case of the above discussed S$_N$2 and induced-inversion channels, basically no product violates ZPE as the ZPE-constrained cross sections are virtually identical with the non-constrained ones, as shown in Fig. 4. This is expected in the case of the highly exothermic S$_N$2 pathways but somewhat surprising in the case of the thermo-neutral induced-inversion channel. This latter finding indicates that induced inversion causes significant internal energy excitation of the reactant by transferring the translational energy into vibrational and rotational degrees of freedom, as will be discussed in more detail later. In the case of the endothermic HF + CH₂Br⁻ channel, ZPE violation is
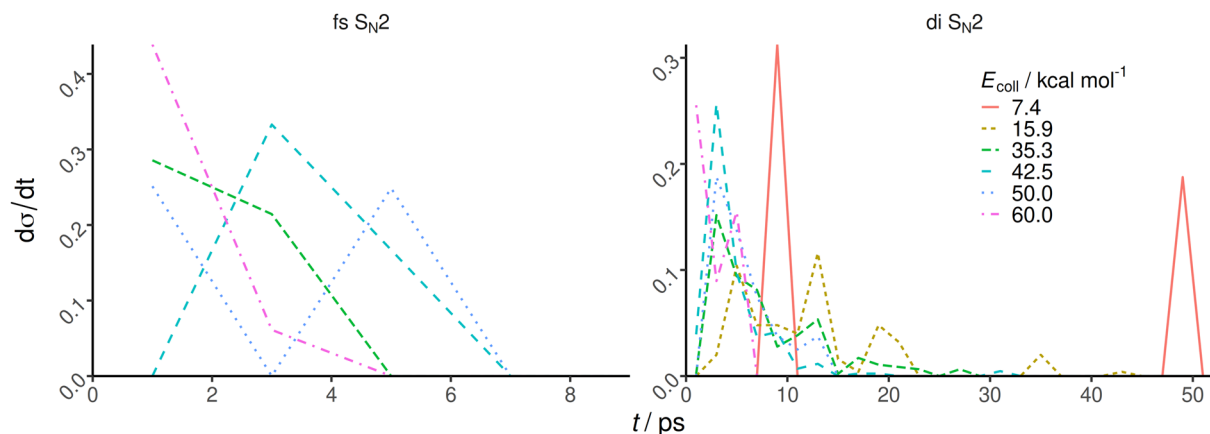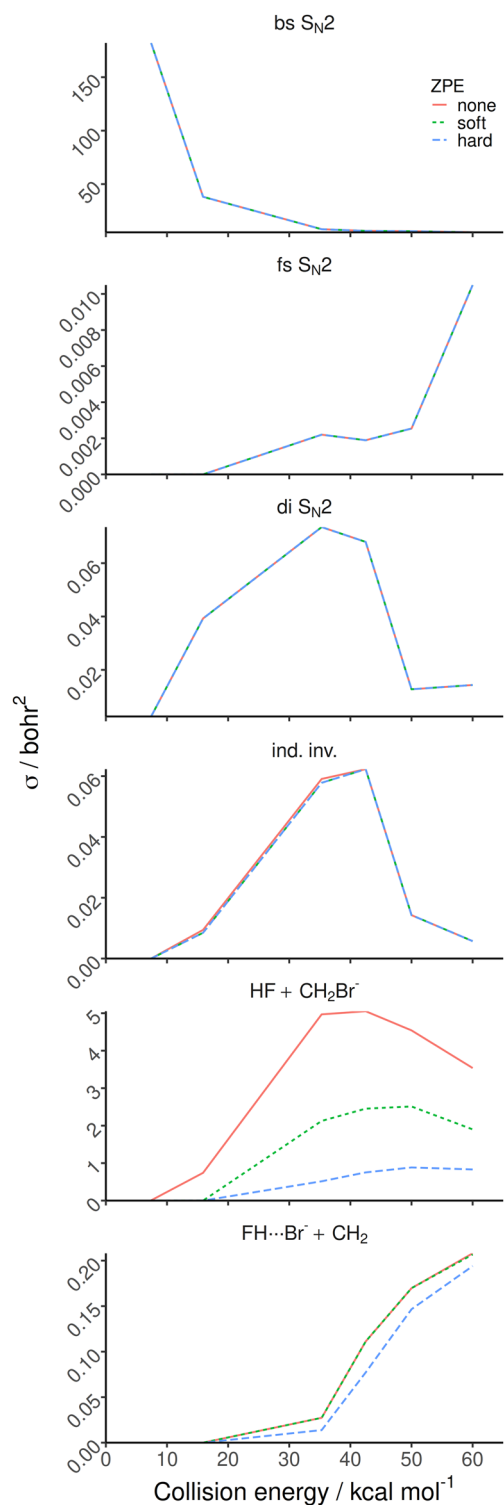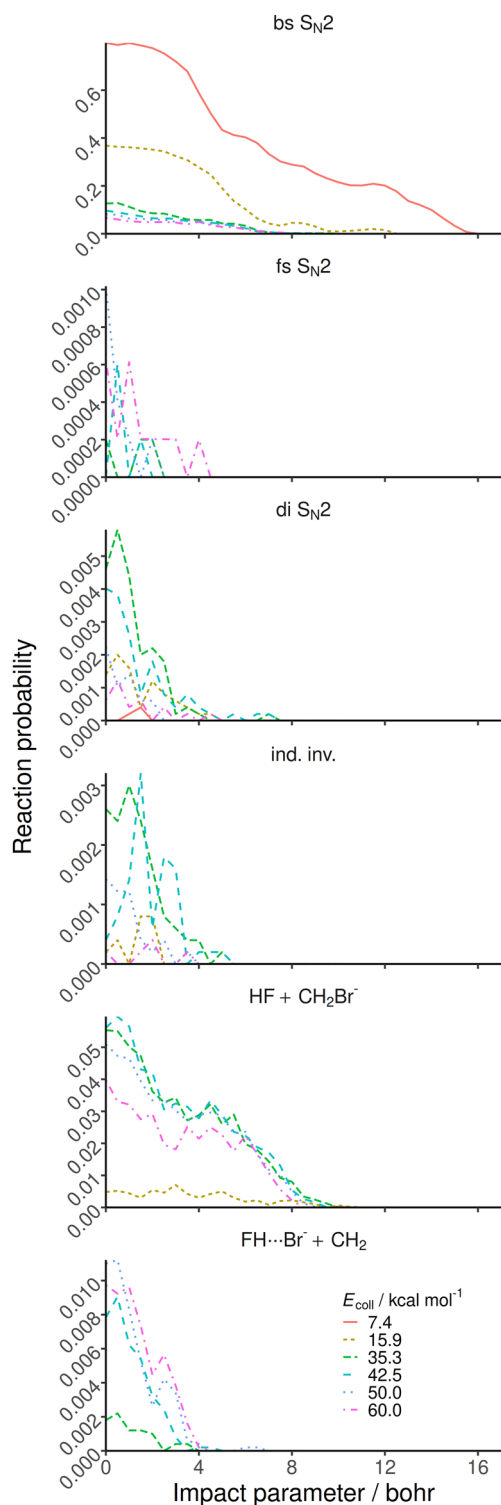

FIG. 3. Integration time distributions for the front-side attack (fs) and double-inversion (di) S$_N$2 pathways of the F⁻ + CH₃Br reaction at different collision energies.

FIG. 4. Cross sections as a function of collision energy for the Walden-inversion (bs), front-side attack (fs), double-inversion (di), induced-inversion (ind. inv.), HF + CH_2Br^-, and FH$\cdots Br^-$ + CH_2 pathways or channels of the F^- + CH_3Br reaction obtained with soft and hard ZPE constraints or without (none) ZPE constraints.

FIG. 5. Reaction probabilities as a function of impact parameter for the Walden-inversion (bs), front-side attack (fs), double-inversion (di), induced-inversion (ind. inv.), HF + CH_2Br^-, and FH$\cdots Br^-$ + CH_2 pathways or channels of the F^- + CH_3Br reaction at different collision energies without ZPE constraints.
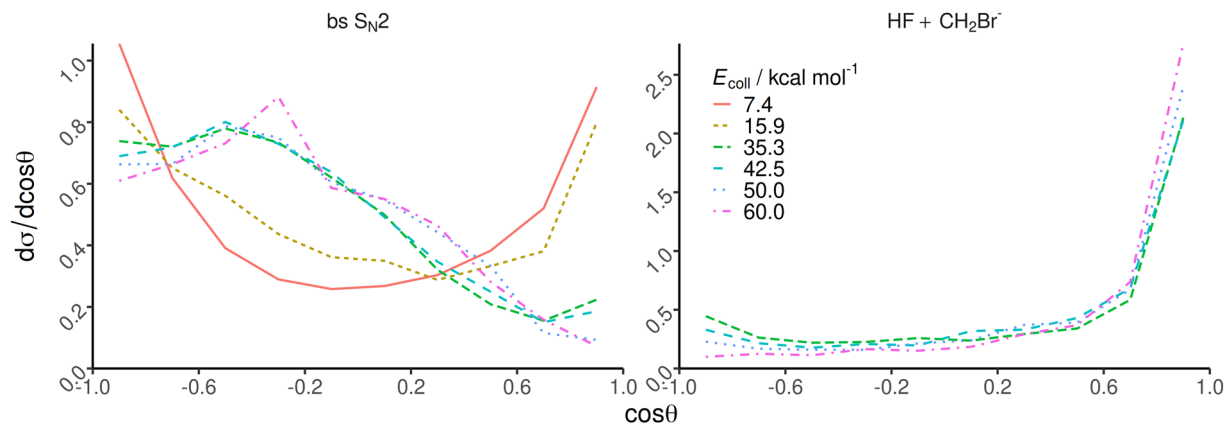
FIG. 6. Normalized scattering angle distributions for the Walden-inversion (bs S_N2) and the proton-abstraction (HF + CH_2Br^-) channels of the F^- + CH_3Br reaction at different collision energies.

more significant. Without ZPE constraints, non-zero cross sections and reaction probabilities are obtained at E_{coll} = 15.9 kcal/mol, below the ΔH_0 value of 20.7 kcal/mol. With soft and hard ZPE constraints, the non-physical reactivity vanishes, as shown in Fig. 4. The non-constrained proton-abstraction cross sections increase with increasing collision energy, reaching a maximum around 40 kcal/mol, and then decrease. A similar excitation-function shape and significantly less reactivity are seen with the soft constraint. Using the hard constraint, the reactivity further decreases, and a nearly constant reactivity is seen at high E_{coll} instead of the decaying behavior. At high collision energies, proton abstraction becomes competitive with the S_N2 channel, for example, at E_{coll} = 60 kcal/mol, the proton-abstraction cross section [3.54, 1.90(soft), 0.83(hard) bohr^2] is similar to the S_N2 cross section (~5 bohr^2). Furthermore, besides the HF + CH_2Br^- products, at E_{coll} = 35.3 kcal/mol, a new product channel forming $FH \cdots Br^-$ + $^1CH_2$ is found in accord with its ΔH_0 value of 33.4 kcal/mol. The cross sections of the $FH \cdots Br^-$ + CH_2 channel increase rapidly with increasing E_{coll}, as also shown in Fig. 4.

Trajectory animations show that $FH \cdots Br^-$ formation begins with a proton abstraction, followed by a Br^- abstraction by the forward moving HF fragment. Note that on the singlet PES, the CH_2 product is formed in the electronically excited singlet state, whereas the ground state of CH_2 is a triplet. However, triplet CH_2 formation would require a non-adiabatic transition between two electronic states (two PESs). We also note that similar complex formation was recently observed experimentally in the case of the F^- + CH_3I reaction.[52] Another high-energy minor product channel is FBr^- + CH_3, but FBr^- formation is not found in our simulations; however, this may be due to the uncertainty of the analytical PES in this region.

Scattering angle (θ) and initial attack angle (α) distributions for the S_N2 and proton-abstraction channels are shown in Figs. 6 and 7, respectively. α is defined at the beginning of each trajectory as the angle between the C–Br vector and the center of the mass velocity vector of CH_3Br. Thus, $\alpha = 0°$ corresponds to front-side attack, whereas $\alpha = 180°$ means back-side attack. For the S_N2
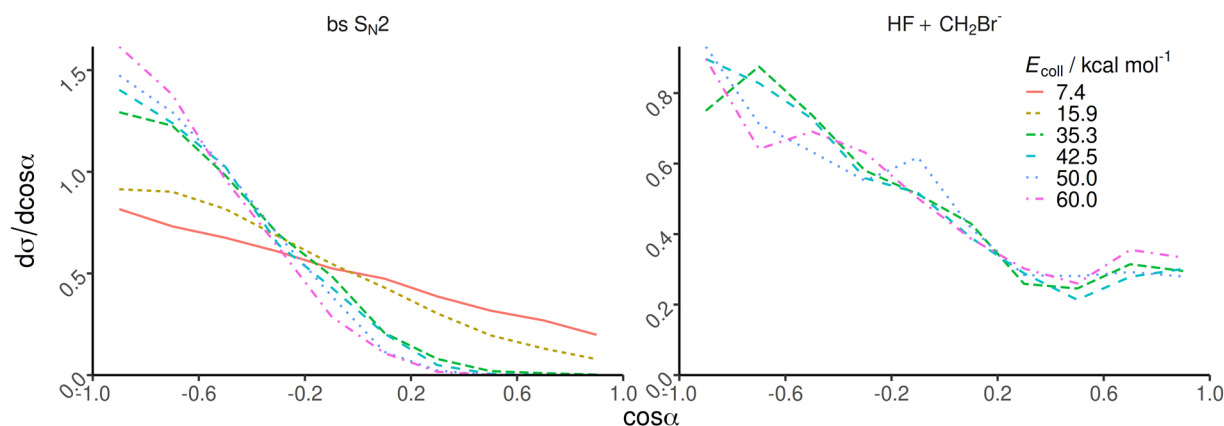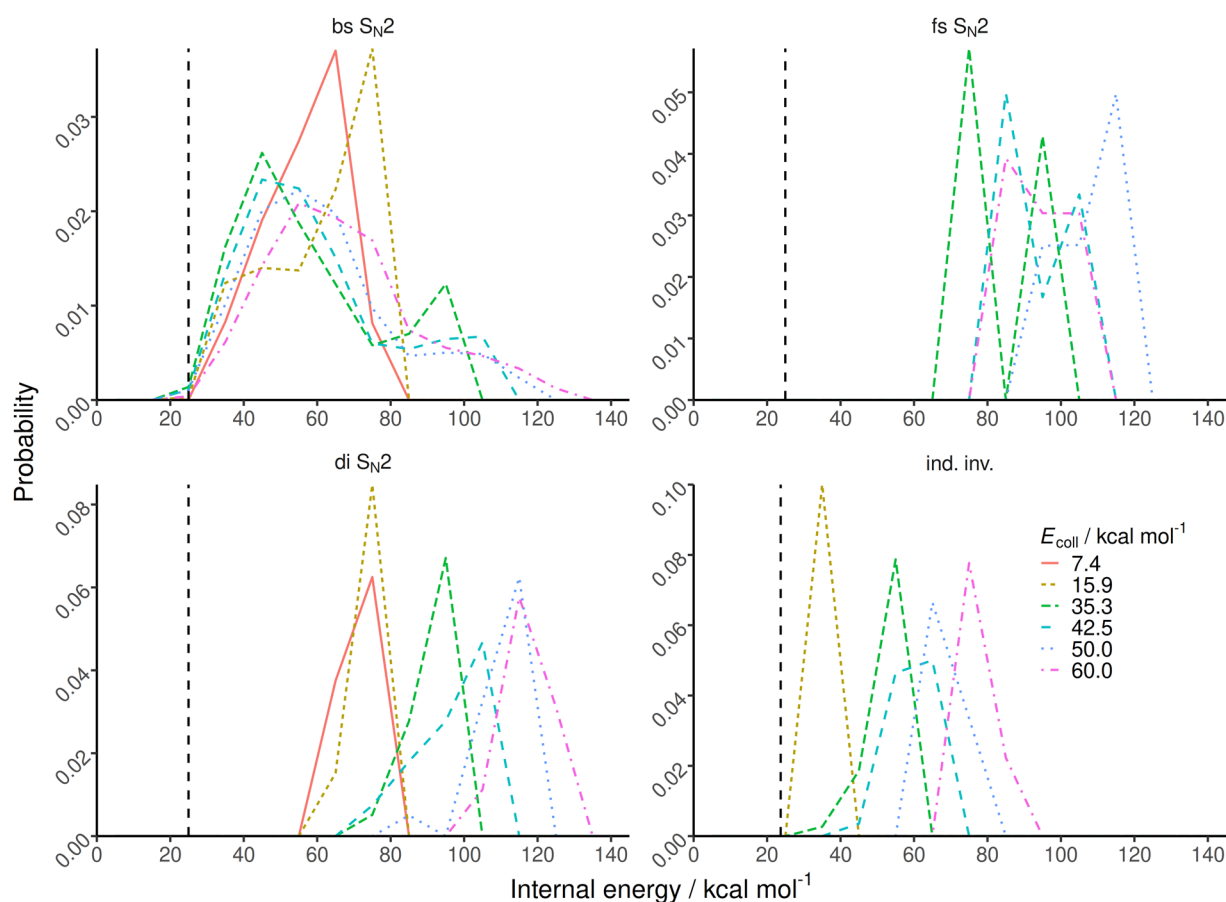

FIG. 7. Normalized initial attack angle distributions for the Walden-inversion (bs S_N2) and the proton-abstraction (HF + CH_2Br^-) channels of the F^- + CH_3Br reaction at different collision energies.

channel, the scattering angle distributions are backward–forward symmetric at low E_{coll} and shift toward backward scattering ($\theta = 180°$) as E_{coll} increases. At $E_{coll} = 35.3$–60.0 kcal/mol, backward scattering clearly dominates. This indicates that at low E_{coll}, direct rebound (backward scattering, small b), direct stripping (forward scattering, large b), and indirect (isotropic scattering) pathways occur, whereas at high E_{coll}, the direct rebound becomes the primary mechanism. This is consistent with the α distributions because at low E_{coll}, a significant fraction of the reactive S_N2 trajectories begins with front-side (Br side) attack, which finally leads to Walden inversion via an indirect pathway. At higher E_{coll}, the initial backside attack, which results in direct rebound, clearly dominates. This finding is similar to the dynamics of the $F^- + CH_3Cl$ S_N2 reaction.[29,41] The proton-abstraction channel shows forward scattering, indicating the dominance of the direct stripping mechanism. The initial attack angle distributions show that it is most likely that proton abstraction occurs when F^- approaches the CH_3 side of the reactant.

Mechanism-specific product internal energy distributions are shown for the S_N2 and induced-inversion channels in Fig. 8. In all cases, the product molecules are vibrationally hot, with basically no

ZPE violation, in accord with Fig. 4. In the case of the Walden-inversion bs S_N2 channel, at low E_{coll}, the CH_3F internal energy distributions peak close to the highest available energies, whereas as E_{coll} increases, the distributions become broader and their peaks shift toward smaller internal energies, indicating a transition from indirect (high internal excitation) to direct (low internal excitation) mechanisms as E_{coll} increases. The product internal energy distributions for front-side attack and double-inversion S_N2 retention pathways and for induced inversion are statistically less converged due to their low reaction probability. Nevertheless, the qualitative trends are clearly visible in Fig. 8. Both front-side attack and double inversion produce highly excited CH_3F products with internal energies close to the maximal available energy at a given E_{coll}. This is consistent with our previous findings that double inversion is an indirect process.[40] In the case of front-side attack, the hot CH_3F products may also be attributed to the fact that the FSTS structure is highly distorted relative to the product geometry, which may cause high product vibrational excitations. We should also emphasize that the front-side attack and double-inversion product internal energy distributions are much hotter than those of the corresponding Walden-inversion S_N2 channel. Induced inversion also provides

FIG. 8. Normalized product internal energy distributions for the Walden-inversion (bs S_N2), front-side attack (fs S_N2), double-inversion (di S_N2), and induced-inversion (ind. inv.) pathways of the $F^- + CH_3Br$ reaction at different collision energies. Dashed vertical lines indicate the ZPEs of the CH_3F (bs, fs, di S_N2) and CH_3Br (ind. inv.) products.
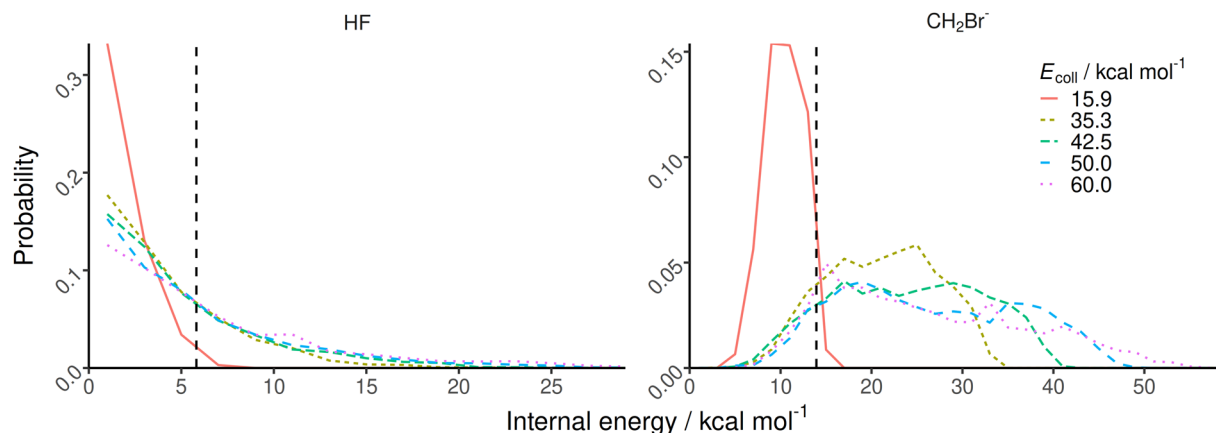
FIG. 9. Normalized product internal energy distributions for the proton-abstraction channel of the $F^- + CH_3Br$ reaction at different collision energies. Dashed vertical lines indicate the ZPEs of the HF and CH_2Br^- products.

highly excited inverted CH_3Br molecules. As shown in Fig. 8, virtually all of the collision energy transfers into internal excitation of the CH_3Br fragment. Furthermore, one can also observe that the internal energy distributions of double and induced inversions are quite similar; just the double-inversion peaks are blueshifted by the excess reaction energy (~40 kcal/mol).

For the HF and CH_2Br^- products of the proton-abstraction channel, the internal energy distributions are shown in Fig. 9. Unlike in the case of the S_N2 channel, the proton-abstraction products are internally cold, with significant ZPE violation. This is especially true for the HF product molecules whose internal energy distributions peak at zero. At the lowest E_{coll} of 15.9 kcal/mol, both the HF and
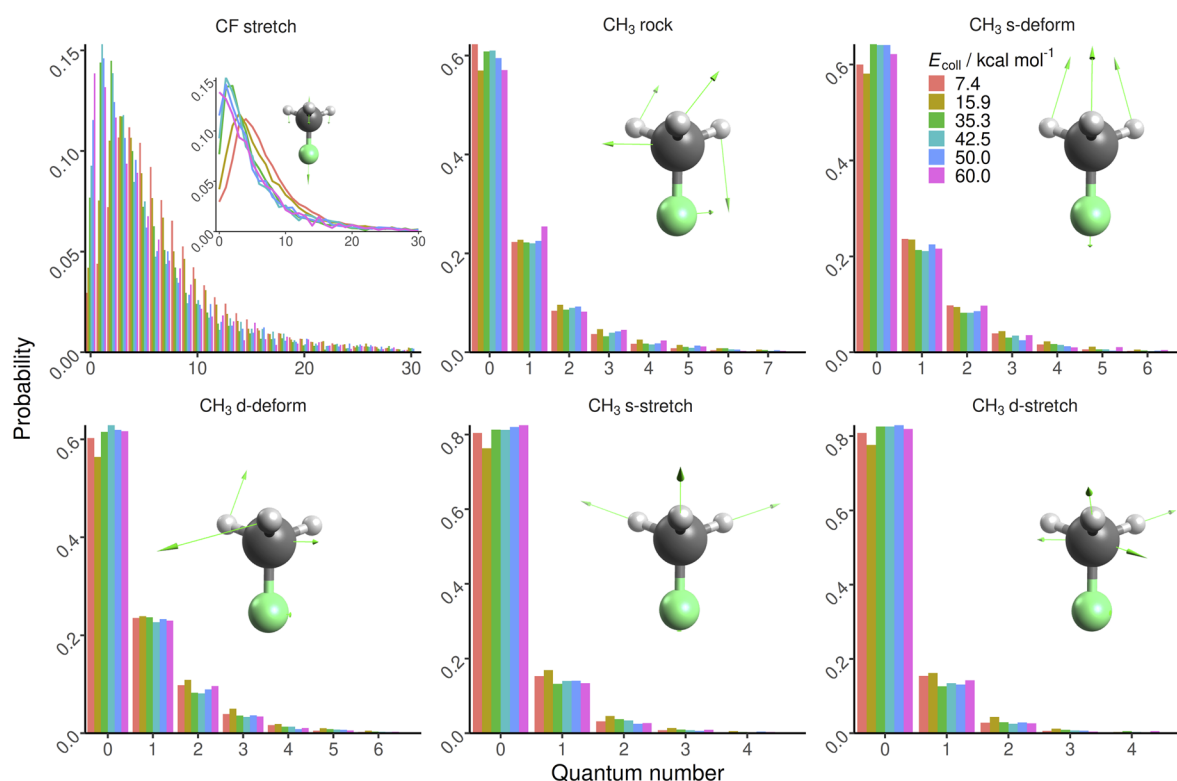
FIG. 10. Normalized mode-specific vibrational distributions for the CH_3F product of the $F^- + CH_3Br$ S_N2 reaction at different collision energies.
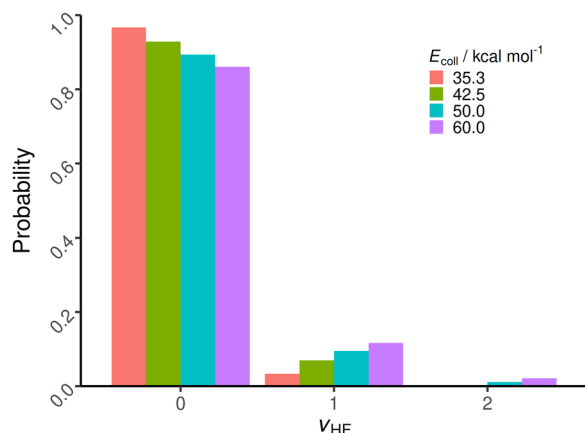
FIG. 11. Normalized vibrational distributions for the HF product of the $F^- + CH_3Br$ proton-abstraction reaction at different collision energies.
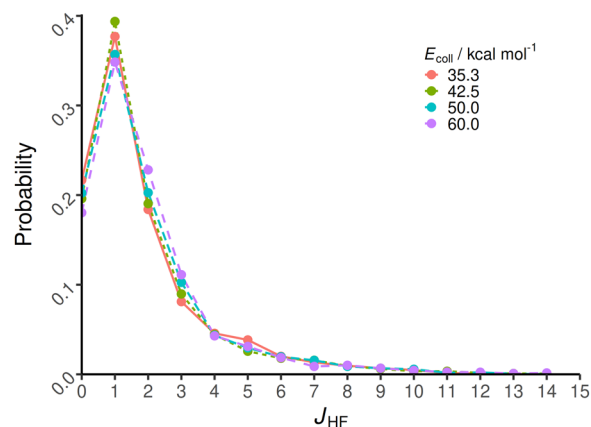

FIG. 12. Normalized rotational distributions for the HF product of the $F^- + CH_3Br$ proton-abstraction reaction at different collision energies.

CH_2Br^- products mainly have classical internal energies below the corresponding ZPE values, as clearly shown in Fig. 9. The CH_2Br^- products are more excited than HF, and the CH_2Br^- distributions are significantly broader than those of the diatomic co-product.

At higher E_{coll}, ZPE violation is still significant for HF whereas small in CH_2Br^-.

Mode-specific vibrational distributions for the CH_3F S_N2 product are shown in Fig. 10. The bending/torsional and CH stretching
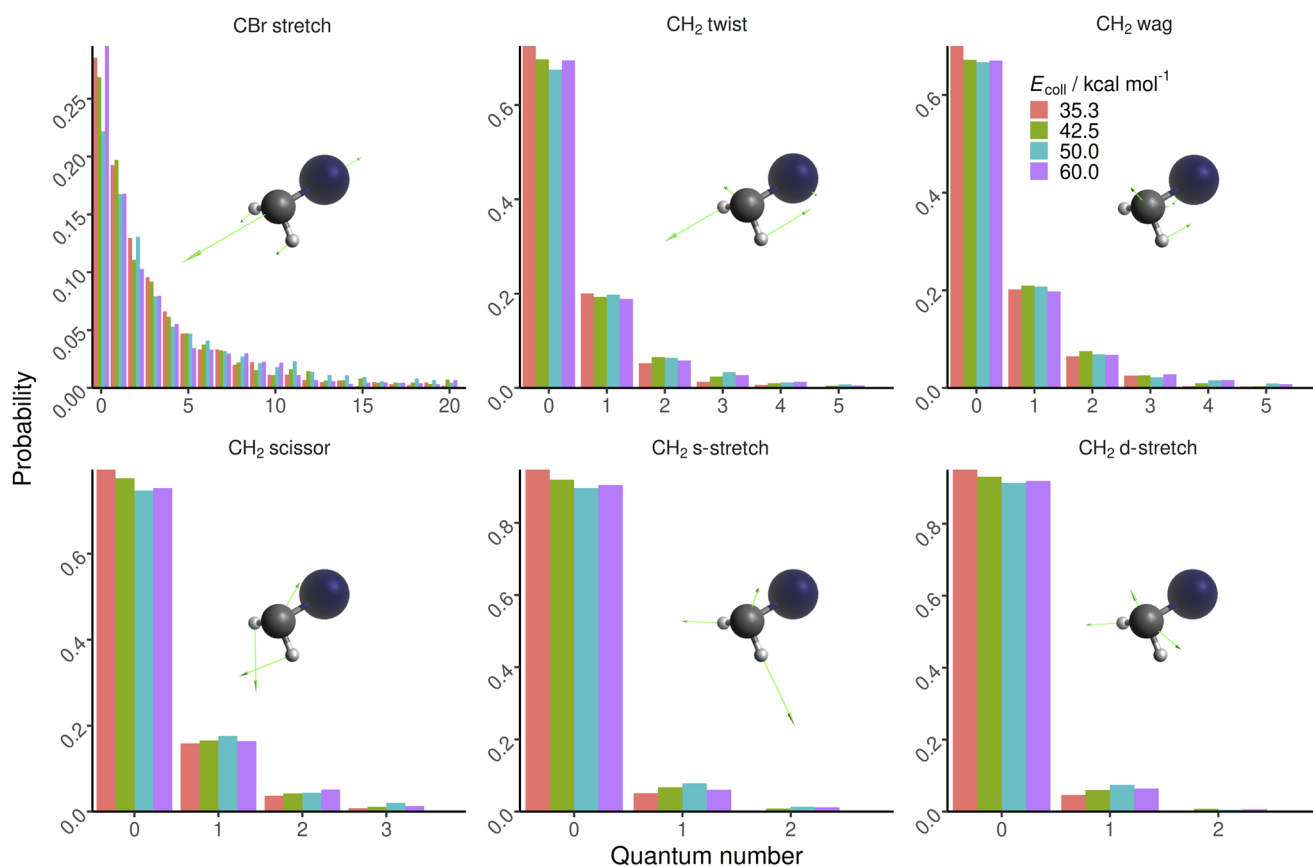

FIG. 13. Normalized mode-specific vibrational distributions for the CH_2Br^- product of the $F^- + CH_3Br$ proton-abstraction reaction at different collision energies.

modes are usually in vibrational ground state with about 60% and 80% probability, respectively, without any significant E_{coll} dependence. Bending/torsional excitations with 1 (20%), 2 (10%), 3 (5%), and 4 (1%–2%) quantum/quanta and CH stretching excitations with 1 quantum (15%) and 2 quanta (5%) are possible with decreasing probability as shown in parentheses, again without significant E_{coll} dependence. In the case of the low-frequency CF stretching mode, substantial populations are seen in the 0–10 quantum number interval, and small probabilities are obtained up to 20–40 quanta excitations. The significant CF stretching excitation is expected in the product because CF is the new bond formed in the S_N2 reaction, and at the WALDENTS, the CF distance is substantially stretched relative to the same bond in the product molecule. Unlike the other product modes, the CF stretching excitation shows E_{coll} dependence; at low E_{coll}, the larger quantum numbers dominate, whereas at high E_{coll}, the lowest CF stretching states are the most populated, showing that the E_{coll} dependence of the CF stretching population is responsible for the redshifting peaks in the CH_3F internal energy distributions upon increasing E_{coll}.

Quantum-number resolved vibrational and rotational distributions for the HF product of the proton-abstraction channel are shown in Figs. 11 and 12, respectively. In accord with the cold internal energy distributions shown in Fig. 9, 97%, 93%, 89%, and 86% of the HF molecules are formed in the ground vibrational state at collision energies of 35.3, 42.5, 50.0, and 60.0 kcal/mol, respectively. Besides the ground state, at the lowest two E_{coll}, only the $v = 1$ state is open, and at the highest two E_{coll}, small $v = 2$ populations (1%–2%) appear, as shown in Fig. 11. The rotational distributions are also cold, peaking at $J = 1$ (35%–40%) and decaying sharply as J increases without any significant E_{coll} dependence. It is interesting to note that these cold HF rotational distributions are reminiscent of the HCl(J) distributions of the Cl + $CH_4/C_2H_6 \rightarrow$ HCl + CH_3/C_2H_5 reactions.[45,53]

Mode-specific vibrational distributions for the CH_2Br^- product ion of the proton-abstraction channel are shown in Fig. 13. The CH stretching modes are usually not excited as their ground state populations are always larger than 89%. The CH_2 twist, wag, and scissor bending modes have similar quantum number populations, i.e., excitation probabilities with 0, 1, and 2 quantum/quanta are around 70%–80%, 15%–20%, and 5%–10%, respectively. The low-frequency CBr stretching mode is also in the vibrational ground state with the highest probability (22%–30%); however, here, higher excitations are also significant with decreasing probabilities, such as 16%–20%, 10%–13%, 7%–10%, 5%–7%, and 3%–5% for 1, 2, 3, 4, and 5 quantum/quanta excitations, respectively. At 10 quanta excitations, the populations are 1%–2%, and at 20 quanta excitations, the probability is less than 1%. Significant E_{coll} dependence is not seen in the mode-specific CH_2Br^- vibrational distributions in the 35.3–60.0 kcal/mol E_{coll} range, and the overall picture shows that the CH_2Br^- product is mainly formed in the vibrational ground state in accord with the cold internal energy distributions shown in Fig. 9.

IV. SUMMARY AND CONCLUSIONS

We have performed a detailed QCT study on the F− + $CH_3Br(v = 0)$ reaction, utilizing our recently-developed full-dimensional analytical *ab initio* PES.[31] Besides the major S_N2 and proton-abstraction channels, cross sections and reaction probabilities are obtained for the minor induced-inversion and FH···Br− + CH_2 channels. Furthermore, for the S_N2 channel, mechanism-specific results are determined for the back-side attack Walden inversion as well as the front-side attack and double-inversion retention pathways. We show that a TS attack angle-based approach can almost unambiguously separate the front-side attack and double-inversion mechanisms. Double inversion is the dominant retention pathway at low collision energies and the first induced inversion, forming an inverted CH_3Br molecule, is followed by a reactive substitution event with about 50% probability. Double inversion is a slow, indirect process, whereas front-side attack is more direct as we also found for the F− + CH_3Y [Y = F, Cl, and I][30,32,40] S_N2 reactions. However, based on the timescale of the two mechanisms, one cannot unambiguously separate them in the case of the F− + CH_3Br reaction like for Y = I and unlike for Y = F and Cl. The Walden-inversion S_N2 channel is indirect at low E_{coll}, and as E_{coll} increases, the direct rebound pathway becomes dominant as the backward scattering, preferential initial back-side attack reactivity, and redshifting product internal-energy peaks indicate. These features are similar to those of the F− + CH_3Cl S_N2 reaction.[29,41] The HF + CH_2Br^- channel is clearly forward scattered showing the dominance of direct stripping with preferential CH_3-side attack as shown by the initial attack angle distributions. For the Walden-inversion S_N2 channel, the mode-specific product vibrational distributions reveal that the E_{coll} dependence of the CF stretching populations is responsible for the redshifting internal energy peaks upon increasing E_{coll}. For the first time, we have also presented internal energy distributions for the front-side attack, double-inversion, and induced-inversion channels of an S_N2 reaction. All distributions are hot and located close to the maximum available energies. The proton-abstraction channel provides internally cold HF and CH_2Br^- products, with significant ZPE violation and clear dominance of the HF($v = 0$ and $J = 1$) and $CH_2Br^-(v = 0)$ states.

The present study demonstrates the current capacity of first-principles reaction dynamics for a six-atomic multi-channel reaction, showing that an analytical PES allows characterizing low-probability reaction channels and computing statistically accurate differential cross section data including mode-specific distributions. In the future, the present PES may be utilized in time-dependent quantum wave packet computations, thereby correctly describing ZPE and tunneling effects. However, the current state-of-the-art of such quantum computations for S_N2 reactions is reduced(6)-dimensional[38] and mainly limited to reaction probabilities and integral cross sections of the major channels. Nevertheless, one may use the one-dimensional Gaussian binning procedure[49,54,55] to incorporate some quantum effects into the quasiclassical mode-specific polyatomic product analysis. Theory may also motivate future experiments on the title reaction and further studies on mode-specificity and/or isotope effects, thereby advancing our current knowledge on the dynamics of fundamental chemical processes.

DATA AVAILABILITY

The data that support the findings of this study are available from the corresponding author upon reasonable request.

REFERENCES

[1] P. Walden, Ber. Dtsch. Chem. Ges. **29**, 133 (1896).

[2] E. D. Hughes and C. K. Ingold, J. Chem. Soc. **1**, 244 (1935).

[3] W. A. Cowdrey, E. D. Hughes, C. K. Ingold, S. Masterman, and A. D. Scott, J. Chem. Soc. **2**, 1252 (1937).

[4] C. K. Ingold, *Structure and Mechanisms in Organic Chemistry* (Cornell University Press, Ithaca, NY, 1953).

[5] D. K. Bohme and L. B. Young, J. Am. Chem. Soc. **92**, 7354 (1970).

[6] J. I. Brauman, W. N. Olmstead, and C. A. Lieder, J. Am. Chem. Soc. **96**, 4030 (1974).

[7] S. E. Barlow, J. M. Van Doren, and V. M. Bierbaum, J. Am. Chem. Soc. **110**, 7240 (1988).

[8] S. T. Graul and M. T. Bowers, J. Am. Chem. Soc. **113**, 9696 (1991).

[9] K. Giles and E. P. Grimsrud, J. Phys. Chem. **96**, 6680 (1992).

[10] A. A. Viggiano and R. A. Morris, J. Phys. Chem. A **100**, 19227 (1996).

[11] P. Kebarle, Int. J. Mass Spectrom. **200**, 313 (2000).

[12] J. Mikosch, S. Trippel, C. Eichhorn, M. Weidemüller, and R. Wester, J. Phys. Chem. A **112**, 10448 (2008).

[13] D. M. Cyr, G. A. Bishea, M. G. Scarton, and M. A. Johnson, J. Chem. Phys. **97**, 5911 (1992).

[14] P. Ayotte, J. Kim, J. A. Kelley, S. B. Nielsen, and M. A. Johnson, J. Am. Chem. Soc. **121**, 6950 (1999).

[15] R. Wester, A. E. Bragg, A. V. Davis, and D. M. Neumark, J. Chem. Phys. **119**, 10032 (2003).

[16] P. B. Armentrout, Int. J. Mass Spectrom. **200**, 219 (2000).

[17] L. A. Angel and K. M. Ervin, J. Phys. Chem. A **105**, 4042 (2001).

[18] J. Mikosch, S. Trippel, C. Eichhorn, R. Otto, U. Lourderaj, J. X. Zhang, W. L. Hase, M. Weidemüller, and R. Wester, Science **319**, 183 (2008).

[19] H. B. Schlegel, K. Mislow, F. Bernardi, and A. Bottoni, Theor. Chim. Acta **44**, 245 (1977).

[20] W. L. Hase, Science **266**, 998 (1994).

[21] G. Li and W. L. Hase, J. Am. Chem. Soc. **121**, 7124 (1999).

[22] L. Sun, K. Song, and W. L. Hase, Science **296**, 875 (2002).

[23] H. Tachikawa and M. Igarashi, Chem. Phys. Lett. **303**, 81 (1999).

[24] H. Tachikawa and M. Igarashi, Chem. Phys. **324**, 639 (2006).

[25] J. Xie, R. Otto, J. Mikosch, J. Zhang, R. Wester, and W. L. Hase, Acc. Chem. Res. **47**, 2960 (2014).

[26] J. Xie and W. L. Hase, Science **352**, 32 (2016).

[27] J.-L. Le Garrec, B. R. Rowe, J. L. Queffelec, J. B. A. Mitchell, and D. C. Clary, J. Chem. Phys. **107**, 1021 (1997).

[28] C. Hennig and S. Schmatz, J. Chem. Phys. **121**, 220 (2004).

[29] I. Szabó, A. G. Császár, and G. Czakó, Chem. Sci. **4**, 4362 (2013).

[30] I. Szabó, H. Telekes, and G. Czakó, J. Chem. Phys. **142**, 244301 (2015).

[31] T. Győri and G. Czakó, J. Chem. Theory Comput. **16**, 51 (2020).

[32] B. Olasz, I. Szabó, and G. Czakó, Chem. Sci. **8**, 3164 (2017).

[33] D. A. Tasi, T. Győri, and G. Czakó, Phys. Chem. Chem. Phys. **22**, 3775 (2020).

[34] D. Papp and G. Czakó, Chem. Sci. **12**, 5410 (2021).

[35] J. Meyer, V. Tajti, E. Carrascosa, T. Győri, M. Stei, T. Michaelsen, B. Bastian, G. Czakó, and R. Wester, Nat. Chem. (published online) (2021).

[36] I. Szabó and G. Czakó, J. Phys. Chem. A **121**, 9005 (2017).

[37] G. Czakó, T. Győri, D. Papp, V. Tajti, and D. A. Tasi, J. Phys. Chem. A **125**, 2385 (2021).

[38] Y. Wang, H. Song, I. Szabó, G. Czakó, H. Guo, and M. Yang, J. Phys. Chem. Lett. **7**, 3322 (2016).

[39] Y. Li, Y. Wang, and D. Wang, J. Phys. Chem. A **121**, 2773 (2017).

[40] I. Szabó and G. Czakó, Nat. Commun. **6**, 5972 (2015).

[41] M. Stei, E. Carrascosa, M. A. Kainz, A. H. Kelkar, J. Meyer, I. Szabó, G. Czakó, and R. Wester, Nat. Chem. **8**, 151 (2016).

[42] I. Szabó, B. Olasz, and G. Czakó, J. Phys. Chem. Lett. **8**, 2917 (2017).

[43] R. Wester, Mass Spectrom. Rev. (published online) (2021).

[44] D. Papp and G. Czakó, J. Chem. Phys. **153**, 064305 (2020).

[45] D. Papp, V. Tajti, T. Győri, and G. Czakó, J. Phys. Chem. Lett. **11**, 4762 (2020).

[46] W. L. Hase, *Encyclopedia of Computational Chemistry* (Wiley, New York, 1998), pp. 399–407.

[47] P. Papp, V. Tajti, and G. Czakó, Chem. Phys. Lett. **755**, 137780 (2020).

[48] G. Czakó, B. C. Shepler, B. J. Braams, and J. M. Bowman, J. Chem. Phys. **130**, 084301 (2009).

[49] G. Czakó, J. Phys. Chem. A **116**, 7467 (2012).

[50] A. Y. Dymarsky and K. N. Kudin, J. Chem. Phys. **122**, 124103 (2005).

[51] K. N. Kudin and A. Y. Dymarsky, J. Chem. Phys. **122**, 224105 (2005).

[52] E. Carrascosa, T. Michaelsen, M. Stei, B. Bastian, J. Meyer, J. Mikosch, and R. Wester, J. Phys. Chem. A **120**, 4711 (2016).

[53] G. Czakó and J. M. Bowman, Science **334**, 343 (2011).

[54] G. Czakó and J. M. Bowman, J. Chem. Phys. **131**, 244302 (2009).

[55] L. Bonnet and J. Espinosa-García, J. Chem. Phys. **133**, 164108 (2010).